Available online at www.sciencedirect.com
ScienceDirect
Photonics and Nanostructures – Fundamentals and Applications xxx (2015) xxx–xxx
PHOTONICS AND NANOSTRUCTURES Fundamentals and Applications
www.elsevier.com/locate/photonics

Dual-band plasmonic resonator based on Jerusalem cross-shaped nanoapertures

Arif E. Cetin [a,b,c], Sabri Kaya [a,d], Alket Mertiri [e], Ekin Aslan [d], Shyamsunder Erramilli [e,f], Hatice Altug [b], Mustafa Turkmen [d,*]

[a] Department of Electrical and Computer Engineering, Boston University, Boston, MA 02215, USA
[b] Bioengineering Department, Ecole Polytechnique Federale de Lausanne (EPFL), Lausanne CH-1015, Switzerland
[c] Department of Biological Engineering and Koch Institute for Integrative Cancer Research, Massachusetts Institute of Technology, Cambridge, MA 02139, USA
[d] Electrical and Electronics Engineering, Erciyes University, 38039 Kayseri, Turkey
[e] Division of Materials Science and Engineering, Boston University, Boston, MA 02215, USA
[f] Department of Physics, Boston University, Boston, MA 02215, USA

Received 25 November 2014; received in revised form 5 April 2015; accepted 6 April 2015

Abstract

In this paper, we both experimentally and numerically introduce a dual-resonant metamaterial based on subwavelength Jerusalem cross-shaped apertures. We numerically investigate the physical origin of the dual-resonant behavior, originating from the constituting aperture elements, through finite difference time domain calculations. Our numerical calculations show that at the dual-resonances, the aperture system supports large and easily accessible local electromagnetic fields. In order to experimentally realize the aperture system, we utilize a high-precision and lift-off free fabrication method based on electron-beam lithography. We also introduce a fine-tuning mechanism for controlling the dual-resonant spectral response through geometrical device parameters. Finally, we show the aperture system's highly advantageous far- and near-field characteristics through numerical calculations on refractive index sensitivity. The quantitative analyses on the availability of the local fields supported by the aperture system are employed to explain the grounds behind the sensitivity of each spectral feature within the dual-resonant behavior. Possessing dual-resonances with large and accessible electromagnetic fields, Jerusalem cross-shaped apertures can be highly advantageous for wide range of applications demanding multiple spectral features with strong nearfield characteristics.

Keywords: Plasmonics; Nanofabrication; Metamaterials; Subwavelength optics; Multi-band resonator

1. Introduction

Plasmonic subwavelength systems based on metallic nanoapertures or nanoparticles have received significant attention as they have very advantageous optical properties, which enable extraordinary physical phenomena, e.g., from metamaterials to perfect lensing [1–4]. Recently accessing excitation-forbidden dark modes, systems with extraordinary optical properties have been introduced [5,6]. Electromagnetic properties of plasmonic systems could also result in multi-resonant spectral responses derived from the collective mechanism of

* Corresponding author.
E-mail address: turkmen@bu.edu (M. Turkmen).

http://dx.doi.org/10.1016/j.photonics.2015.04.001
1569-4410/

constituting resonating elements [7–9]. Optical properties of these multi-resonant systems are highly dependent on the refractive index of surrounding media [10], shape and orientation of the apertures [11,12], aperture size [12,13], metal thickness [14], and the lattice geometry of the aperture arrays [15–25]. This dependence provides a fine-tuning mechanism of their multi-resonant spectra in wide wavelength ranges. Recent advancements in computational electromagnetics and nanofabrication techniques enable numerical and experimental analyses of these nanostructures, which provide tunable multi-resonant spectral responses [26–32]. For instance, microwave dual-resonant metamaterials have been introduced for extraordinary refractive index properties [33,34], while near-infrared multi-spectral nanoapertures have been investigated for negative indexing [35,36]. In this sense recently, Jerusalem cross (JC)-shaped nanostructures have been investigated due to their extraordinary far- and nearfield characteristics [37–41].

In this paper, we experimentally and numerically investigate a dual-band resonator system based on JC-shaped aperture arrays. We show the physical origin of the dual-resonant behavior, deriving from the constituting aperture elements in the compact system, through finite difference time domain (FDTD) simulations. We also introduce a fine-tuning mechanism for controlling the dual-resonant optical response via geometrical parameters. We show that the aperture system supports large and highly accessible local electromagnetic fields, significantly improving light-matter interaction in nanometer scale, which is highly important for surface-enhanced applications demanding strong nearfields. We also perform numerical calculations in order to quantitatively show the accessibility of local electromagnetic fields. Highly advantageous nearfield characteristics of the nanoapertures are shown through numerical calculations on refractive index sensitivity, where the system is embedded in different refractive indices of bulk solutions. Finally, we utilize a high-precision and lift-off free fabrication method based on electron beam lithography to experimentally realize JC-shaped apertures. Possessing a dual-resonant spectral response with large and accessible nearfields, JC-shaped apertures can be highly advantageous for wide range of applications including ultra-sensitive biosensing and spectroscopy, wavelength-tunable active filters, optical modulators, and ultrafast optical switching devices.

2. Dual-band JC-shaped nanoaperture system

The proposed JC-shaped aperture system is schematically illustrated in Fig. 1a. Aperture arrays are fabricated through a 50 nm gold film standing on a 100 nm free-standing silicon nitride membrane. Fig. 1b shows the scanning electron microscopy (SEM) image of the aperture system, where the device parameters are: $s = 600$ nm, $g = 470$ nm, $w = 200$ nm, $L = 1150$ nm and $P = 1400$ nm (array period). Fig. 1c and d shows the calculated and

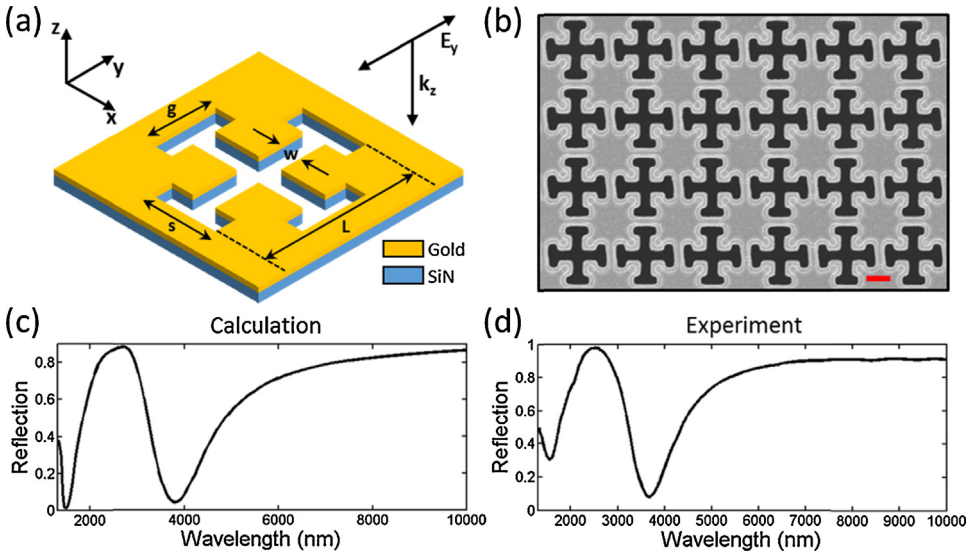

Fig. 1. (a) Schematic illustration of the JC-shaped aperture. In figure, geometrical device parameters of the aperture system along with the polarization and propagation directions of the illumination source are shown. (b) SEM image of the fabricated aperture array. Scale bar, 500 nm. (c) Numerical and (d) experimental reflection spectra of the JC-shaped aperture. Corresponding device parameters are: $s = 600$ nm, $g = 470$ nm, $w = 200$ nm, $L = 1150$ nm, and $P = 1400$ nm. Thicknesses of the silicon nitride (SiN) membrane and gold film are 100 nm and 50 nm, respectively.

Please cite this article in press as: A.E. Cetin, et al. Dual-band plasmonic resonator based on Jerusalem cross-shaped nanoapertures, Photon Nanostruct: Fundam Appl (2015), http://dx.doi.org/10.1016/j.photonics.2015.04.001

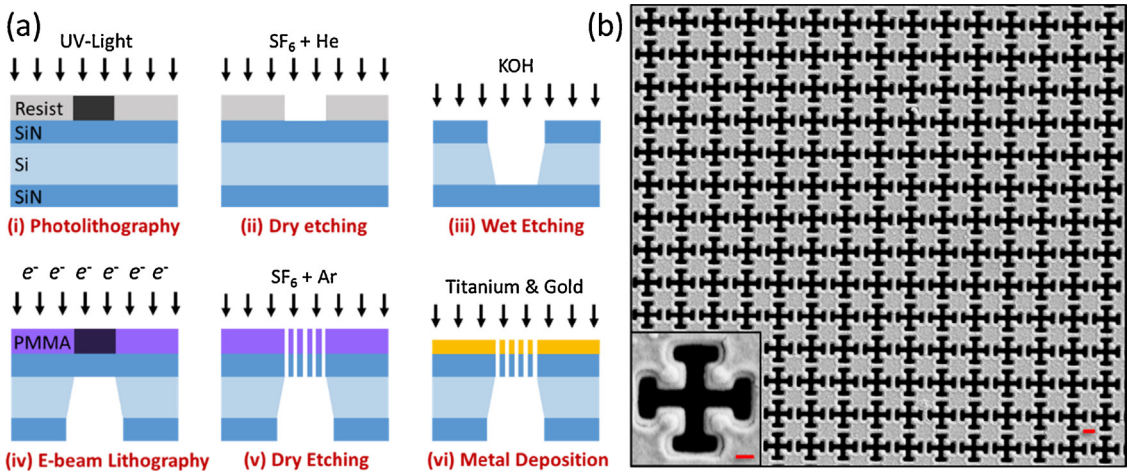

Fig. 2. (a) Steps of the lift-off free nanofabrication method. (b) SEM images of the fabricated nanoapertures. Scale bar (zoom image), 500 nm (200 nm). Corresponding device parameters are: $s = 600$ nm, $g = 470$ nm, $w = 200$ nm, $L = 1150$ nm, and $P = 1400$ nm. Thicknesses of the silicon nitride membrane and gold film are 100 nm and 50 nm, respectively.

experimental reflection spectra under a y-polarized light source (parallel to the top and bottom aperture arms), demonstrating their good correlation, where the aperture system supports two distinct resonances within the spectral region of interest. For experimental measurements, we collect the reflection data using a Fourier transform infrared (FTIR) spectrometer (Bruker, IFS 66/s) coupled to an infrared microscope (Bruker, Hyperion 1000) with a resolution of 4 cm^{-1}, which consists of 256 scans co-added with a mirror repetition rate of 40 kHz. In order to eliminate atmospheric water vapor absorption within the spectral region of interest, data collection is performed under a dry air purged environment. Reflection spectrum is determined through the ratio between the reflected light from the aperture system and the reflected light from a perfect mirror made of an optically thick gold film.

3. Fabrication of JC-shaped apertures

For experimental realization, we utilize a lift-off free nanofabrication technique based on electron-beam lithography, as schematically illustrated in Fig. 2a. We utilize a 500 μm silicon wafer with 100 nm low-pressure chemical vapor deposited (LPCVD) silicon nitride films on both sides. (i) We perform photolithography on a 2 μm positive photoresist (MICROPOSIT^{TM} S1818) using SUSS MicroTec MA/BA6 Mask Aligner. After development, we have 750 μm × 750 μm square aperture patterns on the bottom silicon nitride film. (ii) We perform dry etching (Plasma-Therm Reactive Ion Etcher) using SF_6 and He gases in order to completely remove the silicon nitride film within the transferred pattern at the back side of the wafer. (iii) Chips are then immersed in KOH solution to selectively remove the silicon substrate under the top silicon nitride film. (iv) We perform electron-beam lithography (Zeiss SUPRA 40VP) on a positive resist, polymethyl methacrylate (950 PMMA A5, MICROCHEM). (v) After development on the patterned PMMA using methyl isobutyl ketone and isopropyl alcohol (MIBK-IPA, 1:3) solution, we perform dry etching (while utilizing PMMA as a mask) with SF_6 and Ar gases in order to remove silicon nitride film, which realizes apertures through free-standing silicon nitride membranes. (vi) Finally, we deposit 5 nm titanium (adhesion layer) and 50 nm gold (CHA Electron Beam Evaporator), which realizes apertures through the gold film in a lift-off free manner. SEM images of the fabricated system in Fig. 2b demonstrates that the apertures are well-defined and smooth (zoomed image) as well as the aperture array is uniform over large areas.

4. Origin of dual-resonant response

In order to show the physical origin of the dual-resonant behavior, we perform numerical analyses through FDTD calculations. In simulations, dielectric constants of gold and titanium are taken from Ref. [42] and that of silicon nitride is experimentally obtained through ellipsometry measurements. For the unit cell consisting of a single JC-shaped aperture, periodic boundary condition is used along x- and y-directions in order to create the array behavior (aperture array is along xy-plane) and perfectly matched layer boundary condition is used along z-direction (direction of propagation). Mesh sizes are 5 nm in all directions

Please cite this article in press as: A.E. Cetin, et al. Dual-band plasmonic resonator based on Jerusalem cross-shaped nanoapertures, Photon Nanostruct: Fundam Appl (2015), http://dx.doi.org/10.1016/j.photonics.2015.04.001

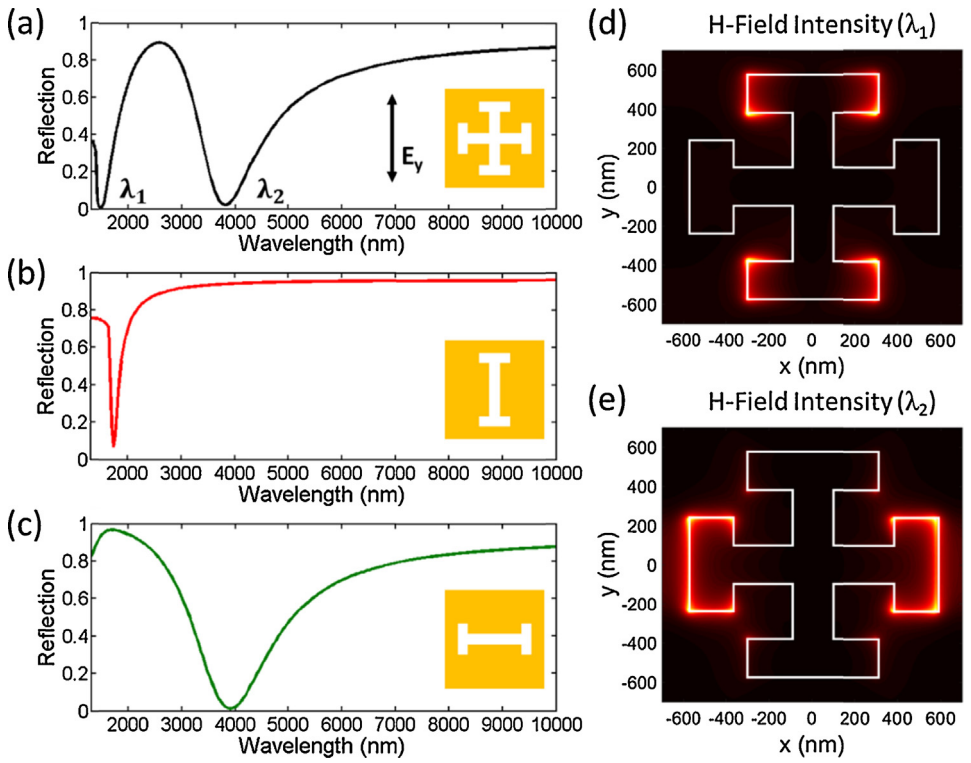

Fig. 3. Calculated reflection spectra of (a) the compact JC-shaped aperture, and the constituting (b) vertical and (c) horizontal H-shaped apertures. Figure inset shows the polarization direction of the illumination source. Magnetic field intensity ($|H|^2$) distributions for the JC-shaped aperture calculated at (d) $\lambda_1 = 1490$ nm and (e) $\lambda_2 = 3800$ nm. Corresponding device parameters are: $s = 600$ nm, $g = 470$ nm, $w = 200$ nm, $L = 1150$ nm, and $P = 1400$ nm. Thicknesses of the silicon nitride membrane and gold film are 100 nm and 50 nm, respectively.

[43,44]. The dual-resonant behavior ($\lambda_1 \sim 1490$ nm and $\lambda_2 \sim 3800$ nm) shown in Fig. 3a is due to the superposition of the spectra of the constituting vertical (Fig. 3b) and horizontal (Fig. 3c) H-shaped apertures. In the composite aperture system, these individual responses shift to shorter wavelengths, where $\lambda_{vertical} = 1740$ nm and $\lambda_{horizontal} = 3900$ nm, respectively. Magnetic field intensity distributions ($|H|^2$) calculated at the dual-resonances in the composite system clearly demonstrate the origin of the dual-resonant behavior, i.e., at λ_1 (λ_2), highly enhanced local electromagnetic fields mainly concentrate at the top and bottom aperture arms (left and right aperture arms).

5. Quantification of nearfield intensity

Fig. 4a and b shows the electric field intensity enhancement distribution ($|E|^2$) for the dual-modes at λ_1 and λ_2, respectively. For the mode at shorter wavelengths, highly enhanced local electromagnetic fields are mainly concentrated at the top and bottom aperture arms with an intensity enhancement factor as large as ~500. In contrast, for the mode at longer wavelengths, they localize along the long axis of the horizontal aperture, with an intensity enhancement factor of ~900. **Fig.** 4c and d shows the ***yz***-cross-sectional profile for the electric field intensity enhancement calculated at $x = 100$ nm (where the electric field intensities are maximum), demonstrating that highly enhanced local electromagnetic fields are homogeneously distributed along the aperture wall through ***z***-direction, while their intensities gradually decreases along *y*-direction.

We then quantitatively demonstrate the accessibility of these local electromagnetic fields, which is highly important for applications demanding strong nearfield properties. Here, we integrate the electric field intensity within a volume (V), where the intensity drops to a cut-off value. Since the maximum intensity for the mode at λ_1 is smaller than the one at λ_2, we set $1/e^2$ of the electric field intensity of the mode at λ_1 as the cut-off [45]. Table 1 shows volume and the corresponding integral of the nearfield intensities calculated within it. Here, the mode at λ_2 supports ~18 times larger volume. Considering the additional effect of the larger nearfield intensity enhancement, the mode at λ_2 has ~20 times larger integral value compared to the mode at λ_1.

Please cite this article in press as: A.E. Cetin, et al. Dual-band plasmonic resonator based on Jerusalem cross-shaped nanoapertures, Photon Nanostruct: Fundam Appl (2015), http://dx.doi.org/10.1016/j.photonics.2015.04.001

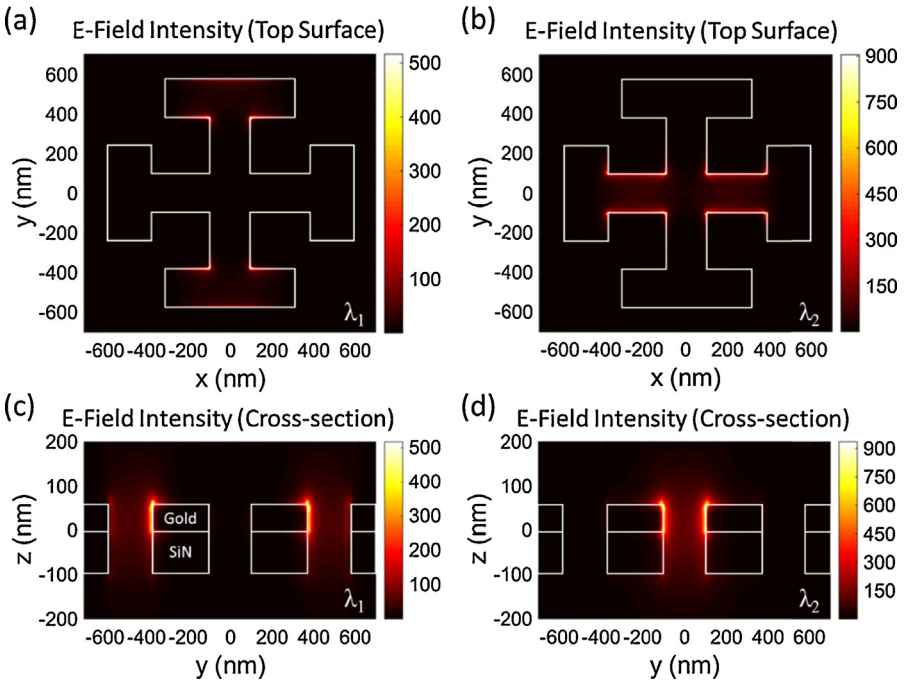

Fig. 4. Electric field intensity enhancement distribution ($|E|^2$) for the JC-shaped aperture calculated at $\lambda_1 = 1490$ nm and $\lambda_2 = 3800$ nm (a,b) at the top gold surface and (c,d) through cross-section. Corresponding device parameters are: $s = 600$ nm, $g = 470$ nm, $w = 200$ nm, $L = 1150$ nm, and $P = 1400$ nm. Thicknesses of the silicon nitride membrane and gold film are 100 nm and 50 nm, respectively.

Table 1
Cut-off volume and the integral of the electric field intensity enhancement over the cut-off volume for the mode locating at λ_1 and λ_2.

	Cut-off volume (V)	$\iiint_V Intensity \times dV$
Mode at λ_1	64,500 nm^3	49,182
Mode at λ_2	1,197,250 nm^3	989,500

6. Fine-tuning of dual-resonant spectra through the aperture geometry

Fig. 5 summarizes the dependence of the dual-resonant spectral response on geometrical parameters. Fig. 5a shows the variations within the plasmonic modes for different L values, where other parameters are kept constant at: $s = 600$ nm, $g = 470$ nm and $w = 200$ nm. Spectral response of the rectangular shaped apertures has a linear dependence on their side, which is perpendicular to the polarization direction of the illumination source as investigated earlier [46]. Therefore, for the mode at λ_2 where the local electric fields are concentrated at the horizontal rectangular aperture along the x-axis, changing L significantly alters this mode and shifts it to longer wavelengths for larger L. In contrast, for the mode at λ_1, since there is no field localization at the vertical H-shaped aperture, we do not observe any spectral variations. Fig. 5b shows the variations within the plasmonic modes for different g values where other parameters are kept constant at: $s = 600$ nm, $L = 1150$ nm and $w = 200$ nm. As for the mode at λ_2, local magnetic fields are concentrated at the left and right aperture arms, increasing g shifts this modes to longer wavelengths. On the other hand, as the mode at λ_1 localizes at the aperture arms along the vertical direction, varying g does not alter this mode. Fig. 5c shows the variations within the plasmonic modes for different s values where other parameters are kept constant at: $g = 470$ nm, $L = 1150$ nm and $w = 200$ nm. Varying s has an opposite effect compared to g on spectral variations. Here, as for the mode at λ_1, local magnetic fields are concentrated at the top and bottom aperture arms, increasing s shifts this modes to longer wavelengths. In contrast, as the mode at λ_2 localizes at the aperture arms along the horizontal direction, varying s does not alter this mode. Here, even though changing s and g results in identical variations in the aperture geometry, the spectral shifts within the mode at λ_2 (due to the variations in g) are larger than those within the mode at λ_1 (due to the variations in s). This is due to the larger intensity integral supported by the mode at λ_2, which is directly proportional to the sensitivity of the system to the change in the surface conditions. Fig. 5d shows the variations within the plasmonic modes for different w values where other

Please cite this article in press as: A.E. Cetin, et al. Dual-band plasmonic resonator based on Jerusalem cross-shaped nanoapertures, Photon Nanostruct: Fundam Appl (2015), http://dx.doi.org/10.1016/j.photonics.2015.04.001

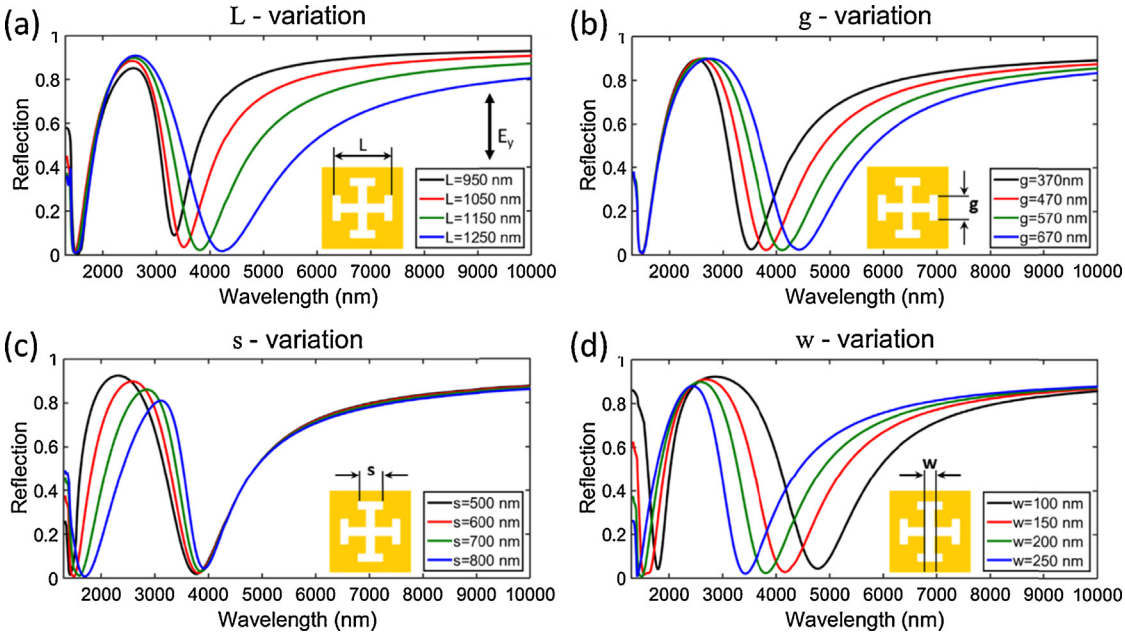

Fig. 5. Spectral variations within the calculated reflection spectra of the JC-shaped aperture for different geometrical parameters. (a) *L*-variation, where $s = 600$ nm, $g = 470$ nm, $w = 200$ nm. Figure inset shows the polarization direction of the illumination source. (b) *g*-variation, where $s = 600$ nm, $L = 1150$ nm, $w = 200$ nm. (c) *s*-variation, where $g = 470$ nm, $L = 1150$ nm, $w = 200$ nm. (d) *w*-variation, where $s = 600$ nm, $g = 470$ nm and $L = 1150$ nm. Thicknesses of the silicon nitride membrane and gold film are 100 nm and 50 nm, respectively, and $P = 1400$ nm.

parameters are kept constant at: $s = 600$ nm, $g = 470$ nm and $L = 1150$ nm. Here, both modes shift to shorter wavelengths for larger w values, where the spectral shift for the mode at λ_2 is larger than that of at λ_1, which is due to two factors. First, increasing this parameter decreases the length of the horizontal aperture, at where the local electric fields are mainly concentrated for the mode at λ_2. Second, even though changing w varies all aperture geometry identically, as the mode at λ_2 supports larger integral value, it varies stronger compared to the mode at λ_1. Therefore, the results presented in this section clearly show that by changing the geometrical parameters, we can precisely tune the spectral responses for realizing aperture systems working in the desired wavelength ranges.

7. Sensitivity of the dual-resonant response

Supporting highly accessible large local electromagnetic fields, JC-shaped aperture system significantly improves light-matter interaction in nanometer scale, which is highly important for surface-enhanced applications demanding strong nearfields [47–49]. As an example to highlight this advantageous nearfield characteristic, we demonstrate numerical calculations on refractive index sensitivity, where the aperture system is embedded in different refractive indices of bulk solutions: DI-water ($n = 1.3325$), acetone ($n = 1.3591$), isopropyl alcohol, IPA ($n = 1.3776$) and glycerol ($n = 1.4722$). Fig. 6a shows the variations within the spectral response of the aperture system, demonstrating that as the refractive index increases, plasmonic modes shift to longer wavelengths. Here, as the mode at λ_2 shows stronger sensitivities (due to larger near-field integral values) compared to the one at λ_1, it shows larger spectral shifts. In order to show the sensitivity character of each mode, we calculate refractive index sensitivity, defined as the ratio between the change in the resonance wavelength and the change in the refractive index of the adjacent medium ($S = \Delta\lambda/\Delta n$). Fig. 6b shows the linear dependence of the resonance wavelength of each plasmonic mode to the refractive index of the bulk medium. These results clearly show that the mode at λ_2 (green line) shows stronger refractive index sensitivities (calculated by taking the derivative of each linear λ, n function) compared to the one at λ_1 (red line), ~2968 nm/RIU vs. ~1285 nm/RIU (RIU = refractive index unit). Supporting dual-resonances with linewidths (full-width-half-maximum, FWHM), 463 nm and 1161 nm for the modes at λ_1 and λ_2, the aperture system support figure-of-merit values ($FOM = S/FWHM$), 2.8 and 2.6, respectively. These values are quite comparable

Please cite this article in press as: A.E. Cetin, et al. Dual-band plasmonic resonator based on Jerusalem cross-shaped nanoapertures, Photon Nanostruct: Fundam Appl (2015), http://dx.doi.org/10.1016/j.photonics.2015.04.001

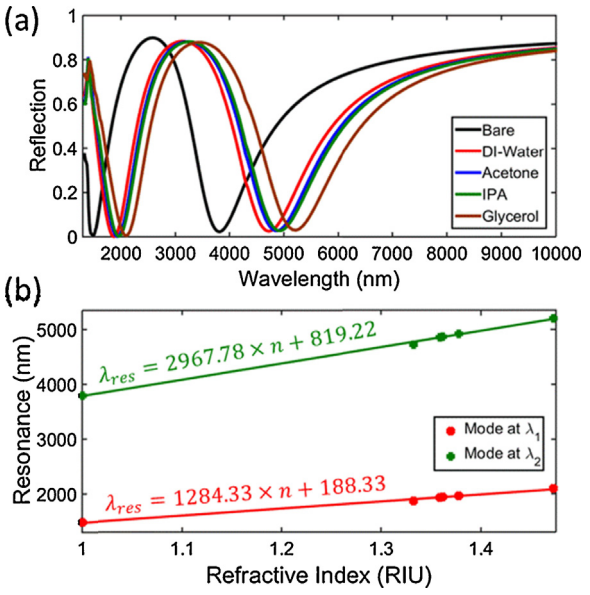

Fig. 6. (a) Spectral variations within the calculated aperture response for different refractive indices of bulk solutions: DI-water ($n = 1.3325$), acetone ($n = 1.3591$), IPA ($n = 1.3776$) and glycerol ($n = 1.4722$). (b) Linear dependence between resonance wavelengths (λ_{res}) of the dual-plasmonic modes and refractive indices. Corresponding device parameters are: $s = 600$ nm, $g = 470$ nm, $w = 200$ nm, $L = 1150$ nm, and $P = 1400$ nm. Thicknesses of the silicon nitride membrane and gold film are 100 nm and 50 nm, respectively.

with the state of the art label-free plasmonic biosensors designed for mid-IR region shown before [50,51].

8. Conclusion

In conclusion, we introduce a dual-resonant metamaterial based on Jerusalem cross (JC)-shaped nanoapertures. We numerically investigate the physical origin of the dual-resonant behavior which is due to the individual spectral response of the constituting aperture elements. For experimental realization, we utilize a high-precision and lift-off free fabrication method based on electron-beam lithography. We also introduce a fine-tuning mechanism for controlling the spectral response of the aperture system through geometrical device parameters. We perform refractive index sensitivity calculations in order to numerically show the aperture system's sensitive nature to the changes in the surface conditions. Finally, the quantitative analyses on the overlap between local electromagnetic fields and the medium in the vicinity of the aperture system show the good correlation between sensitivity of each mode and accessibility of optical fields. Possessing a multi-resonant spectral behavior with easily accessible large local electromagnetic fields, JC-shaped nanoapertures can be a highly good candidate for large variety of surface enhanced optical applications.

Acknowledgements

Turkmen Research Group acknowledges the Technological Research Council of Turkey (TUBITAK) under research grants and project 113E277. Altug Research Group acknowledges Ecole Polytechnique Federale de Lausanne (EPFL).

References

[1] J.B. Pendry, D. Schurig, D.R. Smith, Controlling electromagnetic fields, Science 312 (2006) 1780–1782.
[2] V.M. Shalaev, Optical negative-index metamaterials, Nat. Photonics 1 (2007) 41–48.
[3] C.M. Soukoulis, S. Linden, M. Wegener, Negative refractive index at optical wavelengths, Science 315 (2007) 47–49.
[4] J.B. Pendry, A.J. Holden, D.J. Robbins, W.J. Stewart, Magnetism from conductors and enhanced non-linear phenomena, IEEE Trans. Microw. Theory Tech. 47 (1999) 2075–2084.
[5] A. Jain, P. Tassin, T. Koschny, C.M. Soukoulis, Large quality factor in sheet metamaterials made from dark dielectric meta-atoms, Phys. Rev. Lett. 112 (2014) 117403.
[6] A.E. Cetin, A. Artar, M. Turkmen, A.A. Yanik, H. Altug, Plasmon induced transparency in cascaded π-shaped metamaterials, Opt. Express 19 (2011) 22607–22618.
[7] J.B. Pendry, Metamaterials in the sunshine, Nat. Mater. 5 (2006) 599–600.
[8] A.E. Cetin, M. Turkmen, S. Aksu, D. Etezadi, H. Altug, Multi-resonant compact nanoaperture with accessible large near-fields, Appl. Phys. B 118 (2015) 29–38.
[9] M. Turkmen, S. Aksu, A.E. Cetin, A.A. Yanik, H. Altug, Multi-resonant matematerials based on UT-shaped nano-aperture antennas, Opt. Express 19 (2011) 7921–7928.
[10] T.J. Kim, T. Thio, T.W. Ebbesen, D.E. Grupp, H.J. Lezec, Control of optical transmission through metals perforated with subwavelength hole arrays, Opt. Lett. 24 (1999) 256–258.
[11] A.A. Yanik, X. Wang, S. Erramilli, M.K. Hong, H. Altug, Extraordinary midinfrared transmission of rectangular coaxial nanoaperture arrays, Appl. Phys. Lett. 93 (2008) 081104.
[12] T. Thio, H.F. Ghaemi, H.J. Lezec, P.A. Wolff, T.W. Ebbesen, Surface-plasmon-enhanced transmission through hole arrays in Cr films, J. Opt. Soc. Am. B 16 (1999) 1743–1748.
[13] A.K. Azad, Y. Zhao, W. Zhang, Transmission properties of terahertz pulses through an ultrathin subwavelength silicon hole array, Appl. Phys. Lett. 86 (2005) 141102.
[14] A. Degiron, H.J. Lezec, W.L. Barnes, T.W. Ebbesen, Effects of hole depth on enhanced light transmission through subwavelength hole arrays, Appl. Phys. Lett. 81 (2002) 4327.
[15] T.W. Ebbesen, H.J. Lezec, H. Ghaemi, T. Thio, P.A. Wolff, Extraordinary optical transmission through sub-wavelength hole arrays, Nature 391 (1998) 667–669.
[16] A.V. Itagi, D.D. Stancil, J.A. Bain, T.E. Schlesinger, Ridge waveguide as a near-field optical source, Appl. Phys. Lett. 83 (2003) 4474.

Please cite this article in press as: A.E. Cetin, et al. Dual-band plasmonic resonator based on Jerusalem cross-shaped nanoapertures, Photon Nanostruct: Fundam Appl (2015), http://dx.doi.org/10.1016/j.photonics.2015.04.001

[17] E.X. Jin, X. Xu, Finite-difference time-domain studies on optical transmission through planar nano-apertures in a metal film, Jpn. J. Appl. Phys. 43 (2004) 407–417.
[18] E.X. Jin, X. Xu, Enhanced optical near field from a bowtie aperture, Appl. Phys. Lett. 88 (2006) 153110.
[19] M. Huang, A.A. Yanik, T.Y. Chang, H. Altug, Sub-wavelength nanofluidics in photonic crystal sensors, Opt. Express 17 (2009) 24224–24233.
[20] A.A. Yanik, M. Huang, A. Artar, T.Y. Chang, H. Altug, Integrated nanoplasmonic–nanofluidic biosensors with targeted delivery of analytes, Appl. Phys. Lett. 96 (2010) 021101.
[21] S. Aksu, A.A. Yanik, R. Adato, A. Artar, M. Huang, H. Altug, High-throughput nanofabrication of plasmonic infrared nanoantenna arrays for vibrational nanospectroscopy, Nano Lett. 10 (2010) 2511–2518.
[22] S. Kaya, Windmill-shaped subwavelength apertures operating in the mid-IR regime, IEEE Trans. Nanotechnol. 13 (2014) 1250–1256.
[23] M. Turkmen, Characterization of x-shaped nanoaperture antenna arrays operating in mid-infrared regime, Chin. Opt. Lett. 11 (2013) 070501.
[24] A.F. Coskun, A.E. Cetin, B.C. Galarreta, D.A. Alvarez, H. Altug, A. Ozcan, Lensfree optofluidic plasmonic sensor for real-time and label-free monitoring of molecular binding events over a wide field-of-view, Sci. Rep. 4 (2014) 6789.
[25] A.E. Cetin, A.F. Coskun, B.C. Galarreta, M. Huang, D. Herman, A. Ozcan, H. Altug, Handheld high-throughput plasmonic biosensor using computational on-chip imaging, Light: Sci. Appl. 3 (2014) e122.
[26] S. Lal, S. Link, N.J. Halas, Nano-optics from sensing to waveguiding, Nat. Photonics 1 (2007) 641–648.
[27] M.L. Brongersma, Plasmonics: engineering optical nanoantennas, Nat. Photonics 2 (2008) 270–272.
[28] U. Kreibig, M. Vollmer, Optical Properties of Metal Clusters, Springer, New York, 1995.
[29] E.S. Unlu, R.U. Tok, K. Sendur, Broadband plasmonic nanoantenna with an adjustable spectral response, Opt. Express 19 (2011) 1000–1006.
[30] H.R. Raether, Surface Plasmons on Smooth and Rough Surfaces and on Gratings, Springer, New York, 1988.
[31] J. Kundu, F. Le, P. Nordlander, N.J. Halas, Surface enhanced infrared absorption spectroscopy (SEIRA) using infrared resonant nanoshell aggregate substrates, Chem. Phys. Lett. 452 (2008) 115–119.
[32] R. Bukasov, J.S. Shumaker-Parry, Silver nanocrescents with infrared plasmonic properties as tunable substrates for surface enhanced infrared absorption spectroscopy, Anal. Chem. 81 (2009) 4531–4535.
[33] H. Chen, L. Ran, J. Huangfu, X. Zhang, K. Chen, T.M. Grzegorczyk, J.A. Kong, Metamaterial exhibiting left-handed properties over multiple frequency bands, J. Appl. Phys. 96 (2004) 5338–5340.
[34] D. Wang, L. Ran, B.I. Wu, H. Chen, J. Huangfu, T.M. Grzegorczyk, J.A. Kong, Multi-frequency resonator based on dual-band S-shaped left-handed material, Opt. Express 14 (2006) 12288–12294.
[35] D.H. Kwon, D.H. Werner, A.V. Kildishev, V.M. Shalaev, Near-infrared metamaterials with dual-band negative-index characteristics, Opt. Express 15 (2007) 1647.
[36] U.K. Chettiar, A.V. Kildishev, H.K. Yuan, W. Cai, S. Xiao, V.P. Drachev, V.M. Shalaev, Dual-band negative index metamaterial: Double negative at 813 nm and single negative at 772 nm, Opt. Lett. 32 (2007) 1671.
[37] C.H. Tsao, R. Mittra, Spectral-domain analysis of frequency selective surfaces comprised of periodic arrays of cross dipoles and Jerusalem crosses, IEEE Trans. Antennas Propag. 32 (1984) 478–486.
[38] M. Hosseinipanah, Q. Wu, Equivalent circuit model for designing of Jerusalem cross-based artificial magnetic conductors, Radioengineering 18 (2009) 544–550.
[39] E.C. Kinzel, J.C. Ginn, R.L. Olmon, D.J. Shelton, B.A. Lail, I. Brener, M.B. Sinclair, M.B. Raschke, G.D. Boreman, Phase resolved near-field mode imaging for the design of frequency-selective surfaces, Opt. Express 20 (2012) 11986–11993.
[40] M. Lu, W. Li, E.R. Brown, Second-order bandpass terahertz filter achieved by multilayer complementary metamaterial structures, Opt. Express 36 (2011) 1071–1073.
[41] H.T. Chen, J.F. O'Hara, A.J. Taylor, R.D. Averitt, C. Highstrete, M. Lee, W.J. Padilla, Complementary planar terahertz metamaterials, Opt. Express 15 (2007) 1084–1095.
[42] E.D. Palik, Handbook of Optical Constants of Solids, Academic, Orlando, 1985.
[43] A.E. Cetin, M. Turkmen, S. Aksu, H. Altug, Nanoparticle-based metamaterials as multiband plasmonic resonator antennas, IEEE Trans. Nanotechnol. 11 (2011) 208–212.
[44] A.E. Cetin, H. Altug, Fano resonant ring/disk plasmonic nanocavities on conducting substrates for advanced biosensing, ACS Nano 6 (2012) 9989–9995.
[45] A.E. Cetin, D. Etezadi, H. Altug, Accessible local fields with plasmonic nanoantennas on nanopedestals, Adv. Opt. Mater. 2 (2014) 866–872.
[46] R. Adato, A.A. Yanik, J.J. Amsden, D.L. Kaplan, F.G. Omenetto, M.K. Hong, S. Erramilli, H. Altug, Ultra-sensitive vibrational spectroscopy of protein monolayers with plasmonic nanoantenna arrays, Proc. Natl. Acad. Sci. 106 (2009) 19227–19232.
[47] S. Aksu, A.E. Cetin, R. Adato, H. Altug, Plasmonically enhanced vibrational biospectroscopy using low-cost infrared antenna arrays by nanostencil lithography, Adv. Opt. Mater. 1 (2013) 798–803.
[48] A.E. Cetin, FDTD analysis of optical forces on bowtie antennas for high-precision trapping of nanostructures, Int. Nano Lett. 5 (2015) 21–27.
[49] A.E. Cetin, A.A. Yanik, C. Yilmaz, S. Somu, A. Busnaina, H. Altug, Monopole antenna arrays for optical trapping, spectroscopy and sensing, Appl. Phys. Lett. 98 (2011) 111110.
[50] E. Martinsson, M.M. Shahjamali, K. Enander, F. Boey, C. Xue, D. Aili, B. Liedberg, Local refractive index sensing based on edge gold-coated silver nanoprisms, J. Phys. Chem. C 117 (2013) 23148–23154.
[51] Q. Le, P. Bienstman, Enhanced sensitivity of silicon-on-insulator surface plasmon interferometer with additional silicon layer, IEEE Photonics J. 3 (2011) 538–545.

Please cite this article in press as: A.E. Cetin, et al. Dual-band plasmonic resonator based on Jerusalem cross-shaped nanoapertures, Photon Nanostruct: Fundam Appl (2015), http://dx.doi.org/10.1016/j.photonics.2015.04.001